Solar-Terrestrial Physics. 2025, vol. 11, iss. 3, pp. 3–12. DOI: 10.12737/stp-113202501. © 2025 A.T. Altyntsev, N.S. Meshalkina, S.A. Anfinogentov, D.A. Zhdanov, I.I. Myshyakov, E.F. Ivanov, Chengming Tan, Zhao Wu. Published by INFRA-M Academic Publishing House

DOI: 10.12737/stp-113202501

Received March 06, 2025
Accepted May 28, 2025

PROCESSES OF ACCELERATION AND TRANSFER OF ELECTRONS IN A PULSE CIRCULAR RIBBON FLARE

A.T. Altyntsev
Institute of Solar-Terrestrial Physics SB RAS, Irkutsk, Russia, altyntsev@iszf.irk.ru

N.S. Meshalkina
Institute of Solar-Terrestrial Physics SB RAS, Irkutsk, Russia, nata@iszf.irk.ru

S.A. Anfinogentov
Institute of Solar-Terrestrial Physics SB RAS, Irkutsk, Russia, anfinogentov@iszf.irk.ru

D.A. Zhdanov
Institute of Solar-Terrestrial Physics SB RAS, Irkutsk, Russia, zhdanov@iszf.irk.ru

I.I. Myshyakov
Institute of Solar-Terrestrial Physics SB RAS, Irkutsk, Russia, ivan_m@iszf.irk.ru

E.F. Ivanov
Institute of Solar-Terrestrial Physics SB RAS, Irkutsk, Russia, eugenessrt@gmail.com

Chengming Tan
State Key Laboratory of Solar Activity and Space Weather, National Space Science Center CAS, Beijing, China, tanchengming@nssc.ac.cn

Zhao Wu
School of Space Science and Physics, Shandong University, Weihai, China, wuzhao@sdu.edu.cn
Laboratory for Electromagnetic Detection, Institute of Space Sciences, Shandong University, Weihai, China

Abstract. We discuss acceleration and transport of electrons in the circular flare SOL2024-03-25T06:37:00 of the M4.4 X-ray class, characterized by a record-short duration of hard X-ray emission pulse. We have used radio data in the 0.1–40 GHz range, including images of the flare region in the Siberian Radio Heliograph frequency range. Microwave and hard X-ray emissions are generated in the vicinity of the magnetic domain by the interaction of ropes visible at 1600 Å. The impulsive stage ended with a short peak <5 s long, recorded simultaneously at 35 GHz and in the 100–300 keV range. After the peak under ropes, a long loop in the ultraviolet (UV) rises and a broad plasma ejection appears which is directed along the outer spine observed before the flare. Large loops connect the spine and the remote source. There is a broadband microwave source at the remote footpoint at 215 arcsec, with the delay of its maximum from the peak in the flare core being ~5 s, and the electron propagation velocity along the large loops estimated at one-third of the velocity of light. A distinctive feature of the radiation of the remote source was high degree of its circular polarization. The meter flare emission indicates that tops of large loops are filled with non-thermal electrons with large pitch angles. The set of spatial, spectral, and polarization characteristics of microwave sources obtained for the first time is discussed in the context of the known results on the nature of circular ribbon flares.

Keywords: Sun, acceleration mechanisms, microwave bursts, meter bursts, circle ribbon flare.

INTRODUCTION

Recent observations have revealed that among main flares are circular ribbon ones, which occur in a special magnetic configuration with a photospheric magnetic field domain included in an area with fields of opposite magnetic polarity. Above such a domain is a dome separatrix surface at the top of which there is a point with a null magnetic field [Priest, Titov, 1996, Masson et al., 2009, Sun et al., 2013]. From this point, the so-called spines extend into the dome and up from it. Magnetic field vectors in the vicinity of the spines are directed along them and are opposite in sign. The fields near the inner spine are directed away from the photosphere from the center of the domain, and the fields in the vicinity of the outer spine are manifested in EUV (extreme ultraviolet) observations as large-scale loops whose remote footpoints are closed on regions of the photosphere with vertical fields of the same sign as the domain field. The remote footpoints of these loops can be located hundreds of arcsec away from the domain, i.e. from the flare core. Circular ribbon flares are often accompanied by coronal jets, type III radio bursts, coronal mass ejections, shock waves, coronal dimmings, and kink oscillations of coronal loops and filaments (see, for example, the recent review [Zhang, 2024]).

The energy release of circular flares is assumed to occur in the magnetic reconnection processes not only during the interaction between structures within the do-

main, but also in current sheets formed on separatrix surfaces near the null point [Pontin et al., 2013]. Another feature of circular flares is the response to energy release in the flare core in remote sources. The energy for their activation in EUV and radio emissions is transferred by particles and waves. In the case of plasma ejections, the features of circular flares are related to their closed dome magnetic structure. Plasma ejections should be accompanied by a significant change in the topology of the magnetic field above the domain.

One of the underexplored questions in physics of circular flares is the acceleration and transport of particles in the fundamentally three-dimensional topology of energy release regions. To study the processes of electron acceleration, it is natural to use radio data that allows us to record non-thermal electron fluxes in coronal magnetic structures with a plasma density insufficient to detect the free-free X-ray emission of nonthermal electrons. To date, there are relatively few publications on the results of radio observations of circular flares. Meshalkina et al. [2009] discussed the configuration and scenario of two such flares, which were mapped by the Nobeyama Radioheliograph (NoRH [Torii et al., 1979]) at 17 and 34 GHz. The flares under study were driven by the interaction between magnetic ropes located inside the dome separatrix surface. The response to electron acceleration during a flare was ~1 min pulse of hard X-ray emission in the 50–100 keV channel of the satellite RHESSI (Reuven Ramaty High Energy Solar Spectroscopic Imager) and microwave emission at 17 GHz. At that time in the microwave emission there was a remote source with a high degree of circular polarization (up to 50 %) located 120 arcsec from the flare core. The polarization sign of the emission from the remote source corresponded to an extraordinary wave. In the flare examined in [Altyntsev et al., 2022], ~8 s oscillations of microwave emission at a frequency of 5.7 GHz were observed both in the remote source and in the flare core. The emission oscillations in the flare core were explained by modulation of the acceleration process during the interaction between current ropes inside the domain, and the response in the source that was 60 arcsec away was caused by nonthermal electrons coming from the core at a velocity of $(1.5\div2)10^{10}$ cm/s.

A flare with another driver — magnetic reconnection in the vicinity of the null point — has been discussed in [Kumar et al., 2016]. During the flare, ~3 min quasi-periodic pulsations of hard X-ray and microwave emissions were recorded. The authors believe that the oscillations were triggered by variations in electron acceleration in the vicinity of the null point. In that event, the remote source was not identified.

Microwave sources in the circular ribbon flare SOL2014-12-17T04:51 of the M8.7 X-ray class have been examined in more detail [Chen et al., 2019; Lee et al., 2020]. In addition to AIA/SDO data, sequences of radio maps from MUSER (MingantU SpEctral Radioheliograph) [Yan et al., 2009], available in the 1–2 GHz range, and NoRH [Nakajima et al., 1994] were used to study the dynamics of the flare structure. Comparison of fluxes at frequencies of 17 and 34 GHz has shown that at the beginning of the flare the increase in radio emission can be explained by thermal heating of plasma inside the magnetic domain due to reconnection at the magnetic null point. Signs of nonthermal energy release appear during a stepwise increase in the microwave flux a few minutes before the impulsive phase. During the impulsive phase lasting ~10 min, the emission from the rope inside the dome dominates, microwave sources with circular polarization of opposite signs appearing near the rope's footpoints. The remote source was observed on the maps at a frequency of 17 GHz, yet the impulsive phase does not show up in the emission intensity profile of the remote source. The emission flux from the remote source increased gradually during the flare, similar to the increase in EUV emission. This allowed the authors to assume that the microwave emission from a remote source is generated by a bremsstrahlung mechanism. It follows from MUSER maps that the sources emitting at 1.2–2.0 GHz were located above the null point of the magnetic domain.

In our work, we discuss the scenario and dynamics of electron acceleration and transport during the circular flare SOL2024-03-25T06:37 of the M4.4 X-ray class, characterized by a record-short duration of hard emission (~5 s at half-height in the 100–300 keV channel).

INSTRUMENTS

AIA/SDO UV and EUV images and SDO HMI (Helioseismic and Magnetic Imager) magnetograms have been employed to analyze the dynamics of the spatial structure of the flare [Lemen et al., 2012]. Note that the ~12 s periodicity of AIA/SDO observations is insufficient to observe the dynamics of this flare. Moreover, almost all images in all AIA channels were overexposed just during the flare energy release pulse.

Microwave sources were observed by three antenna arrays of the Siberian Radioheliograph (SRH) [Lesovoi et al., 2014; Lesovoi, Kobets, 2017; Altyntsev et al., 2020]. The mapping was carried out by frequency scanning independently in each range (3–6, 6–12, 12–24 GHz) at an interval of 3.5 s. The spatial resolution of the mapping depends on the frequency and local time of observations. In this work, we have used frequencies from 2.8 to 12.2 GHz with beamwidths varying from 23×83 to 10×18 arcsec. Anfinogentov's software package was employed to construct the images [https://radiomag.iszf.irk.ru/books/sibirskii-radiogeliograf/page/sintez-radioizobrazenii-s-pomoshhiu-paketa-srh-synth]. To analyze time profiles of radio emission, we used measurements of the total SRH flux [https://badary.iszf.irk.ru/srhCorrPlot.php].

Integral solar radio emission spectra were measured with a time resolution of 1 s by NoRP (Nobeyama Radio Polarimeters) [Torii et al., 1979] at five frequencies in the range 1.0–17.0 GHz, the Badary Broadband Microwave Spectropolarimeter (BBMS), [Zhdanov, Zandanov, 2011] at 26 frequencies in the range 4–8 GHz.

In our study, we have used spectra from the 50–3000 MHz SRH spectropolarimeter SOLARSPEL with a time resolution of 0.5 s and a frequency resolution of 1 MHz.

Fluxes at high frequencies 35.25–39.75 GHz were available during the impulsive phase in observations from CBS (Chashan Broadband Solar millimeter spectrometer) [Shang et al., 2022, 2023], recording the dynamic spectrum in the range 35–40 GHz. We utilized data with a frequency resolution of 0.5 GHz and a time resolution of 0.537 s.

Integral spectra in the range 1.6–2.0 GHz were obtained with the radio interferometer MUSER-I (China). The MUSER-I frequency range covers 0.4–2.0 GHz [Yan et al., 2016]. The March 25, 2024 event was observed in the left circular polarization with a spectral resolution of 16 MHz and a time resolution of 3.125 ms.

We also employed data from the radio telescope in Learmonth (Australia), which overlaps in time with other radio data. The telescope is part of RSTN (United States Air Force Radio Solar Telescope Network) [Guidice et al., 1981] whose instruments measure intensity at eight frequencies (245, 410, 610, 1415, 2695, 4995, 8800, and 15400 MHz) with a resolution of 1 s.

Hard X-ray fluxes were measured using Fermi/GBM (Fermi Gamma-Ray Burst Monitor) [Meegan et al., 2009] with a time resolution of 1 s.

OBSERVATIONS

The magnetic structure with domain, isolated by a compact region of a positive vertical field, surrounded by fields of reverse polarity, was formed in the southern part of active region (AR) 13615 on March 24. In AIA/SDO images in EUV lines from 10:00 UT on March 24, 2024, a ring structure appeared around the domain and at times a jet (spine) is seen moving away from this structure in a southerly direction. This configuration can be traced continuously until 00:00 UT on March 26, when the domain of the positive field is significantly reduced in size, and the ring structure in EUV lines disappears. No large flares, except for the event under study, were observed during these days.

Figure 1 shows three time points of AR evolution in the vicinity of the magnetic domain. The time hereafter is given in UT. The magnetic structure is seen to develop over time: on March 24, a fragment begins to stand out in the north of the domain, and it separated on the day of the flare. By March 26, this fragment had moved away to the north, and another fragment had separated to the west.

An M4.4 X-ray flare occurred in this structure on March 25, 2024. Soft X-ray emission began to increase at 06:37, and ceased to decrease at 06:48. The peak of the impulsive phase, when a short pulse of hard X-ray emission with photon energy above 100 keV was observed, was recorded at 06:43:24. During the flare, AR

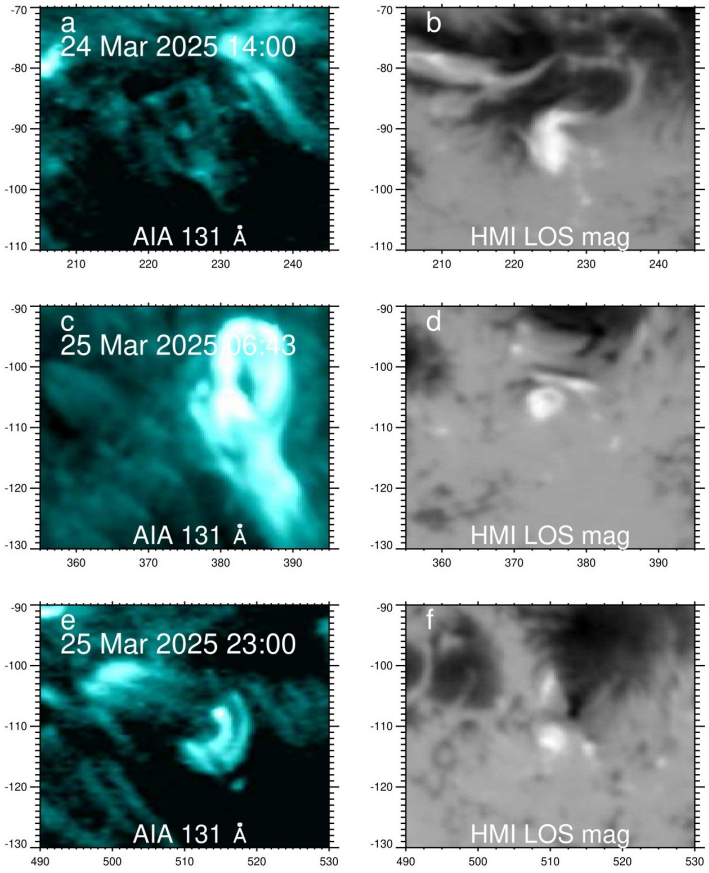

Figure 1. AIA/SDO images in the 131 Å channel at different time points (on the left) and SDO/HMI magnetograms at the time points closest to those indicated in the left column (on the right). On the axes are arcseconds relative to the center of the solar disk

was located in the central part of the solar disk. The flare is noted for its high brightness in all AIA/SDO UV and EUV ranges.

Sequences of unexposed EUV images in the 304 and 131 Å lines during the impulsive phase are shown in Figure 2. At the first two time points, the flare structures have a loop-like shape. Note that a narrow jet extending southward in the plane of the sky was observed for the first time in the 171 Å line at 06:40:57. The jet's brightness and length, which can be considered as a manifestation of the outer spine of the magnetic structure, began to increase after 06:42. Between 06:43:17 and 06:43:30, the jet's transverse size increased significantly, indicating a modification of the magnetic structure near the zero point and the outer spine. Then, the bright region of plasma ejection expanded, with marked fragments elongated along the magnetic field.

The ejection plasma filled large-scale loops, which became visible in EUV emission 4 min after the start of the ejection (Figure 3). In panel *a* at footpoints of large loops, contours depict microwave sources emitting at the maximum of the microwave flux (06:43:24) at a frequency of 8 GHz. In the flare core there is a structure characteristic of a magnetic flux rope: a source in intensity along the edges of which there are sources with different circular polarization. The remote footpoints of the loops were located at a distance of ~215 arcsec east of the flare core in the region with northward magnetic field. Panel *b* shows magnetic field lines calculated by the Green function method in a potential approximation from the HMI/SDO vector magnetogram for 06:48 UT. There is a good agreement between the observed and calculated structures, which allows us to use the calculation results to estimate plasma and magnetic field parameters in large loops.

Let us take a closer look at the structure of the flare core. Figure 4 displays the image in the 131 Å line at 06:43:18 a few seconds before the peak of the hard X-ray emission (*a*); the magnetogram of the longitudinal magnetic field and the image of the flare core in the 1600 Å line at 06:43:26 (*b*). The domain field was positive, its value reached 800 G. The flare was probably

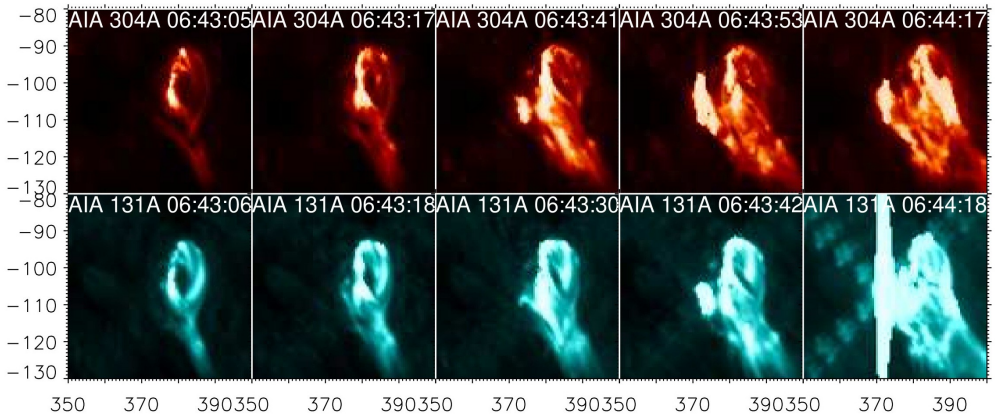

Figure 2. Sequences of images of the flare core in the 304 Å and 131 Å lines. The time is given in UT. The image size is 50×50 arcsec. Image centers are 378/–104 arcsec from the center of the solar disk

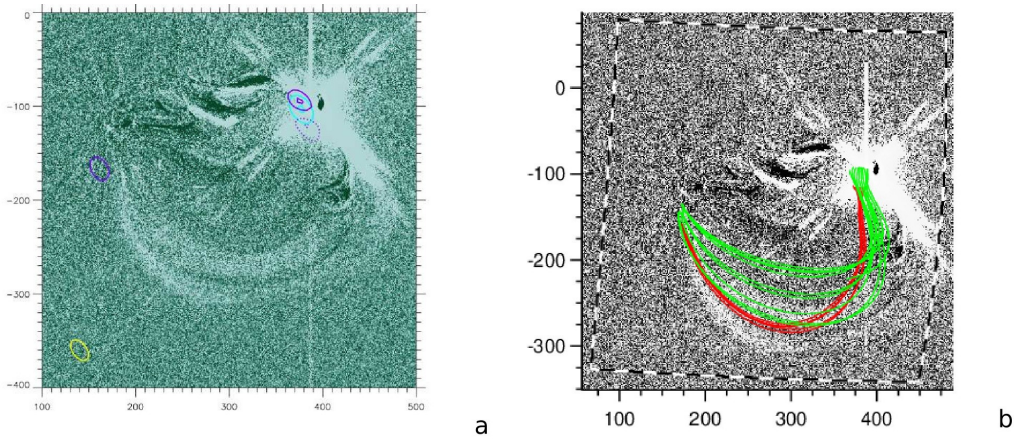

Figure 3. Flare region with a remote source: *a* is the difference image at 06:46 in the 94 Å line. The 06:41 image is subtracted. The contours at the levels (0.5, 0.95) from the maximum/minimum indicate microwave sources. Blue contours show the intensity at a frequency of 8 GHz (SRH); purple, circular polarization: solid contour is the right circular polarization (RCP); dotted, the left circular polarization (LCP). The yellow oval in the lower left corner is the antenna beamwidth at 8 GHz, its size is 15×25 arcsec; green and red lines denote the magnetic field lines calculated in a potential approximation (*b*). The black and white contour is the boundary of the computational domain. The background is a difference image from the left figure

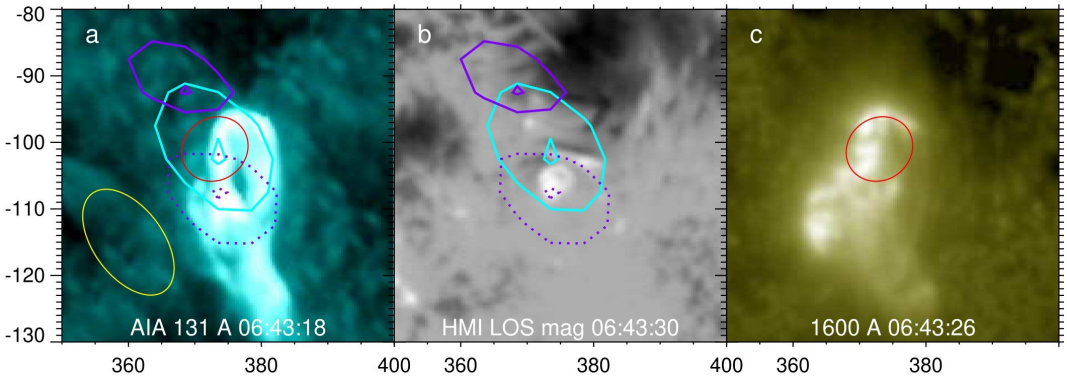

Figure 4. Flare region structure in the 131 Å line at 06:43:18 (*a*); longitudinal magnetic field magnetogram at 06:43:30 (*b*); an image in the 1600 Å line (*c*). The red oval in panels *a*, *c* marks a real source with dimensions 9.3×10.4 arcsec after deconvolution with antenna beamwidth at 12 GHz. The yellow oval in the lower left corner indicates the antenna beamwidth 10.5×18.3 arcsec at 12 GHz. Contours in *a* and *b* outline microwave sources at a frequency of 12 GHz at 06:43:24 in intensity (R+L, blue contour), and polarization (purple contour; solid — RCP (0.5, 0.95 from maximum); dotted — LCP (0.5, 0.95 from minimum))

initiated by separation of a small fragment from the northern part of the domain (see Figure 1, *d*). In EUV emission there is a ring structure in which the brightness depression corresponds to the location of the magnetic domain. The ring's size and shapes are similar in different EUV ranges. In the south, the ring is bordered by a bright region of plasma outflow along the magnetic field lines in the vicinity of the outer spine.

Contours show microwave sources in intensity and polarized microwave emission at a frequency of 12.2 GHz. In the lower left corner, the yellow contour outlines an oval that corresponds to the half-height of the antenna beamwidth. The size of the beamwidth is comparable to the size of the sources. The result of deconvolution under the assumption that the shapes of the pattern and the source are two-dimensional Gaussian functions is depicted by the red oval in panels *a*, *c*. Note that the location of the center of brightness of the microwave source remains unchanged in time. At the edges of the center of brightness in intensity (blue contour) there are sources with opposite directions of circular polarization (purple contours), i.e. the microwave emission structure indicates the existence of loops or ropes.

Panel *c* presents an image in the AIA 1600 Å range almost at the maximum of hard X-ray emission. The main radio source is seen to be above a part of a long flux rope located near the magnetic field domain and extended northwestward. In UV emission, as in EUV emission, southward plasma flow is observed, but the transverse size of the flow has become much wider.

The time profiles of electromagnetic emission of nonthermal electrons accelerated during the flare are presented in Figure 5. High energies of the accelerated electrons are indicated by the microwave emission, recorded with CBS at 35–40 GHz, and by hard X-ray emission, recorded with the FERMI/GBM spectrometer in the 100–300 keV channel. Measurements of the integral solar flux by SRH antennas with a resolution of 3.5 s are given for frequencies of 2.8, 8, and 23.4 GHz. Triangles mark the times of recording at these frequencies. Fluxes at 17 (NoRP), 8.1 GHz (BBMS), and hard X-ray emission intensity (FERMI/GBM) were measured with a resolution of 1 s. The Chinese spectrometer CBS had the best time resolution of 0.5 s.

A noticeable increase in flare emission begins at about 06:42:48 (dash-dotted line) at frequencies below 8 GHz at photon energies below 20 GHz. After 16 s at photon energies to 50 keV, the emission in the range 8–17 GHz begins to increase, reaching a local intensity maximum in 9 s at 06:43:13. In the channels recording harder emissions, the signal begins to grow a few seconds later, at 06:43:19 (dash-dotted line) and reaches a maximum in 5.5 s. In channels of 35 GHz and >50 keV, the signal decreases most rapidly, for 2–3 s, and then the rate of decrease slows down. At the same time, in the top panels of Figure 5, which show the emission of lower-energy electrons, the intensity of signals increases rather than decreases after a pulse of hard emission. Notice that pulses of microwave and hard X-ray emissions are observed at the front of increasing soft X-ray emission whose maximum was recorded at 06:44:35, i.e. more than 1 min later. A similar dependence is characteristic of the Neupert effect when soft X-ray emission is generated by plasma heated by accelerated electron fluxes.

As shown above (see Figure 4, *c*), the microwave source is projected onto a long rope observed in the range of 1600 Å. The dynamics of rope formation can be traced in the images in Figure 6. It can be seen (top row) that before the impulsive phase there are two ropes extended one after another in a northwesterly direction. In the region, where their footpoints approach each other, there is a bright region that rises slightly upward during the impulsive phase. During this phase (middle row), the brightness is distributed along the emerging common flux rope and the region of plasma outflow widens. After the impulsive phase (bottom row), the plasma flow region expands to the length of the rope. The velocity of the leading front of the flow can be estimated from the images in the bottom row as 330 km/s in the plane of the sky.

SRH observations allowed us to identify microwave fluxes from the flare core and remote source. With a distance of 215 arcsec between the sources, the delay between maxima of the time profiles of these sources is ~5 s. Spectra of the sources at the maximum of the impulsive phase are presented in Figure 7, *a*.

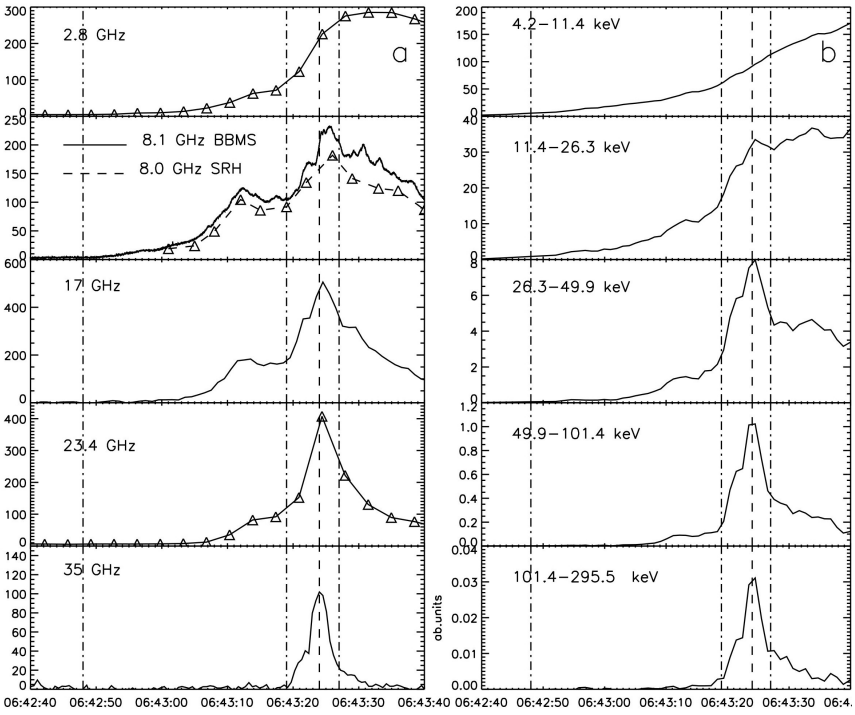

Figure 5. Time profiles of microwave (*a*) and hard X-ray (*b*) emissions. Receiving frequencies and channel boundaries in energies are shown. The instruments in use and the time resolution of the measurements are described in the text. Triangles mark measurement time points at these frequencies in SRH curves of 2.8, 8, and 23.4 GHz. The time points 06:42:48, 06:43:19, 06:43:28 are indicated by vertical dash-dotted lines. The dashed line is the peak of hard X-ray emission at 06:43:24

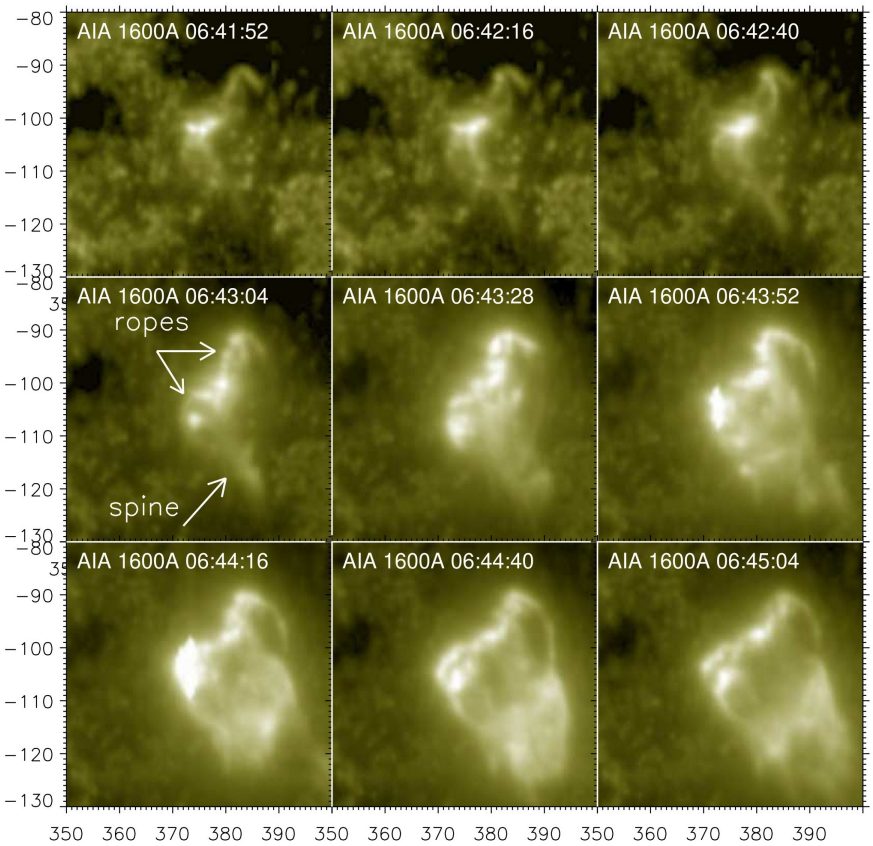

Figure 6. Development of the rope in the flare region; images in the AIA/SDO 1600 Å channel at different time points

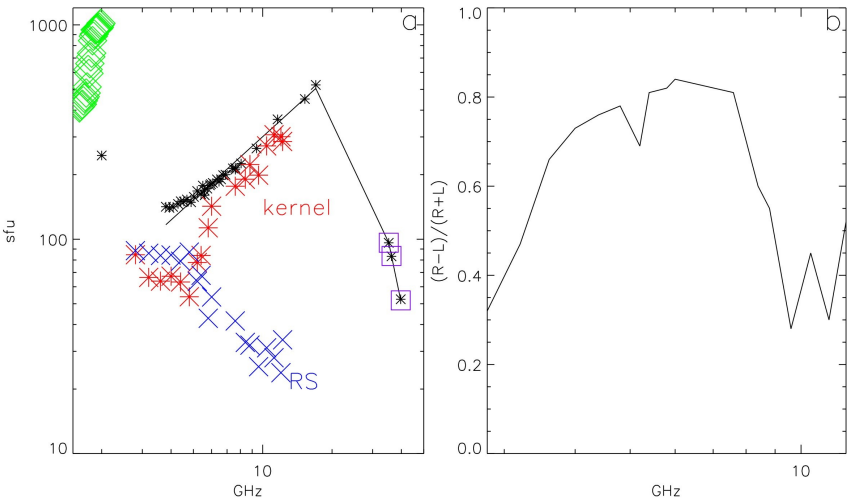

Figure 7. Composite spectrum at the peak of the flare at 06:43:25 (*a*). Red asterisks indicate SRH data, fluxes are collected from images in the flare core; blue crosses, in a remote source; black asterisks mark the integral spectrum from SRH, BBMS, NoRP data; black asterisks in purple squares, CBS data; green rhombs, MUSER-I data. Spectrum of the degree of polarization for a remote source (*b*)

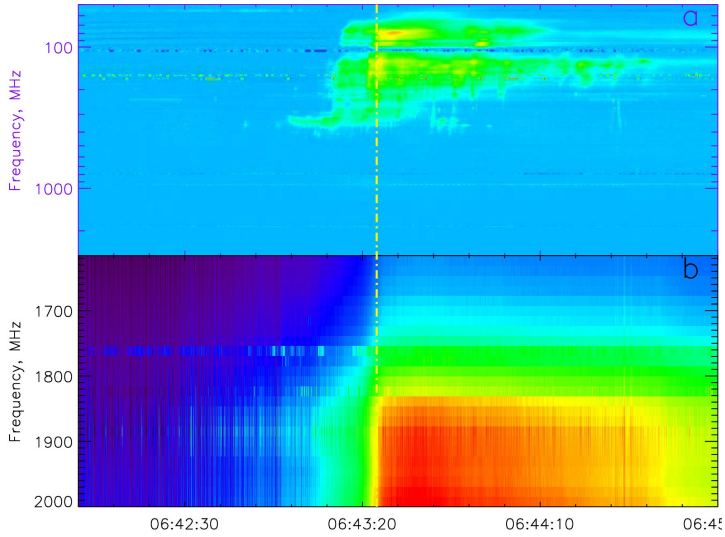

Figure 8. Dynamic spectrum: *a* — data from the 50–3000 MHz SOLARSPEL spectropolarimeter; *b* — MUSER-I data. The vertical line indicates the peak of the hard X-ray emission at 06:43:24

Black asterisks represent the integral flux spectrum from BBMS (4–8 GHz), SRH (11.6 and 15.24 GHz), NoRP (9.4 and 17 GHz), and CBS (35.25, 36.25, 39.75 GHz) data for the peak of the burst at 06:43:24. Since the duration of the peak considered is less than the time resolution of the SRH integral flux curves (3.5 s), not all SRH frequencies could be used for analysis. When constructing the spectrum from SRH data, we selected only those observation frequencies that were within the 0.5 s interval relative to a given time point, which corresponded to the time resolution of CBS data.

The spectrum shape at frequencies above 2 GHz is typical of the gyrosynchrotron spectrum. The core emission becomes dominant in the integral spectrum at frequencies above 6 GHz, and the spectrum index is $f^{1.4}$. The power-law decay index can be described as $f^{-2.5}$. On the contrary, in the remote source spectrum the SRH frequency range covers the decreasing part of spectrum. After the flat part of the spectrum, where the flux from the remote source is comparable to the flux from the flare core, the decrease begins after 4 GHz with $f^{-1.1}$. The next feature of the remote source is a high degree of right circular polarization. In the frequency range from 4.5 to 7.5 GHz, it runs to 80 % (see Figure 7, *b*).

Measurements of the dynamic spectrum at lower frequencies were obtained with the SOLARSPEL spectropolarimeter in the receiving frequency range 50–3000 MHz (Figure 8, *a*). In its dynamic spectrum (*a*), a response to the flare was observed in the frequency range 80–350 MHz. The emission began in a narrow band of ~350 MHz at 06:43:00 and lasted in this band for ~40 s. In a wide band, the emission began at 06:43:10 with maximum intensity during the peak of hard emission. The emission gradually fades, initially at higher frequencies.

Figure 8, *b* displays the MUSER-I dynamic spectrum. The data and figure were obtained using programs developed by Chinese colleagues, including image calibration and improvement [Wang et al., 2013; Tan et al., 2015]. MUSER-I 1600–2000 MHz data shows a flare response in the emission from 1750–2000 MHz. Note that this emission was not recorded in the dynamic spectrum (*a*) due to the lower sensitivity of the 50–3000 MHz SOLARSPEL antenna in the upper part of the operating range (above 1000 MHz). The amplitude of MUSER-I signals increased sharply during the peak. The integral spectrum flux decreased rapidly with decreasing frequency and ceased at frequencies below 1850 MHz (see Figure 8, *b*). There was a slight drift toward low frequencies. Unfortunately, there is a record for this event only in the left polarization of the spectrometer; therefore, the calibrated LCP data was multiplied by two to represent it on the spectrum and compare it with microwave data (see Figure 7, *a*, green rhombs).

DISCUSSION

The data set on the dynamics and spatial structure of the flare makes it possible to define the event under study as a circular ribbon flare with a compact positive field domain in the core and a remote source at the distance of 215 arcsec. The magnetic structure was formed the day before the flare, as evidenced by the appearance of a quasi-stationary circular structure in the EUV emission around the magnetic domain [Masson et al., 2009]. The initiation of the flare impulsive phase is visible in the images of the flare core in the 1600 Å channels: first, a compact bright source appears which is located north of the positive field domain (see Figure 6). It is located at the point of approach of footpoints of two ropes, stretched sequentially in a northwesterly direction. As the flare develops, the ropes become brighter, and after the impulsive phase a long wraparound rope occurs which rises up over time. Simultaneously with the rise of this rope, plasma is seen to flow along the outer spine. A similar scheme for the initiation of a coronal mass ejection has been proposed by Uralov et al. [2002]. It was adopted in [Meshalkina et al., 2009] to explain the initiation of circular ribbon flares.

In our event, dimensions of the SRH antenna beamwidth were comparable to those of the flare core, which makes it impossible to study the interaction between the ropes in microwave emission in more detail. Recording of sources of polarized emission of different signs in the impulsive phase is consistent with the assumption about the formation of a common rope (see Figure 4). The location and brightness of the observable sources of polarized emission result from convolution of the real sources with the SRH antenna beamwidth. Hence, on radio maps the distance between the apparent brightness centers of polarized sources decreases with increasing receiving frequency, i.e. it depends on the size of the antenna bemwidth. At the highest mapping frequency of 12.2 GHz in this work, the SRH spatial resolution (10.4×18.2 arcsec) was insufficient to determine the actual location of the polarized sources.

After the impulsive phase, plasma was seen to flow along large loops oriented along the outer spine. The loops could be observed in difference images of EUV emission a few minutes after the impulsive phase. Figure 3 shows that their observable shape and the location of the remote footpoint are close to the field lines calculated in the potential approximation. It follows from the calculations that the height of the loops is in the range 50–130 Mm with a length 300–400 Mm. To fill the loops with plasma for 4 min, its flow velocity has to be several times higher than the velocity of 330 km/s in the plane of the sky. Estimates suggest that the required flow velocity can be achieved if it is of the order of the velocity of ionic sound at a plasma temperature 20–30 MK in the flare core. A similar propagation mechanism with formation of a heat wave of replacement has been discussed in [Brown et al., 1979; Vlahos, Papadopoulos, 1979; Levin, Melnikov, 1993; Meshalkina, Altyntsev, 2024].

The peak of the emission from the remote source in microwaves lags behind the peak in the flare core by ~5 s. The emission spectrum of the remote source is broadband with a maximum spectrum at a frequency below 4 GHz. The accuracy of determining the delay from SRH data is ~1 s since SRH measurements in the remote source were carried out at an interval of 3.5 s. In the flare core, the accuracy of determining the peak from the 35 GHz profile was fractions of a second. With an average loop length of 350 Mm, we obtain a flight velocity of emitting electrons $\sim 7 \cdot 10^9$ cm/s. The ~17 keV kinetic energy of electrons at this velocity is insufficient to generate the microwave spectrum of the remote source. If we take into account (as is often done [Aschwanden, 2004]) the helicity of magnetic field lines and the pitch angle of propagating electrons, the estimated velocity can be multiplied by 2, then the electron energy becomes more reasonable — ~70 keV. Note that it was the only time such an estimate was obtained for a remote source of a circular flare during observations of quasi-periodic oscillations with SSRT at a high time resolution [Altyntsev et al., 2022]. In this work, we have estimated the energy of emitting electrons at >100 keV.

At sufficiently large pitch angles of electrons propagating along large loops, it is natural to expect their capture at tops of the loops. Their emission can explain the response to the flare in dynamic spectra in the range 80–350 MHz. If we assume that the emission is plasma, the plasma density at loop tops varies in a wide range from $8 \cdot 10^7$ to $1.5 \cdot 10^9$ cm^{-3}. Calculations give 10–20 G magnetic fields, i.e. the observed frequencies are within 3–6 harmonics of the cyclotron frequency of electrons. In this case, it is natural to expect that the emission will be generated at double plasma resonance [Ledenev, 1998; Zheleznyakov et al., 2016].

In the flare core and the remote source, the spectra are gyrosynchrotron with different power-law decay indices f^{β}. A harder spectrum with β=–1.1 was observed in the remote source. Estimated power-law index of electron energy distribution δ by the formula $\beta = 1.22 - 0.9\delta$ [Dulk, Marsh, 1982] yields $\delta \approx 2.5$. A feature of the microwave emission from the remote source is a high

degree of circular polarization up to 80 %. According to calculations of the gyrosynchrotron spectrum in [Fleishman, Melnikov, 2003], such a high degree of polarization indicates large pitch angles of emitting electrons. On the other hand, for large pitch angles the above estimate for isotropic electron distribution $\delta\approx2.5$ can only be considered as a first approximation and requires refinement.

For the flare core, observations with the spectropolarimeters gave an estimate of the slope of the spectrum $\beta\approx-2.5$, from which we get $\delta\approx4.1$. Unfortunately, SRH observations were available to the frequency of 12.2 GHz, i.e. only in the rising spectrum part. The power-law growth index $\beta\approx1.4$ is two times lower than the calculated value of the gyrosynchrotron spectrum emitted by a homogeneous source.

Short growth and decay fronts of the hard peak of microwave and hard X-ray emissions suggest that acceleration to energies above 100 keV occurred in the open configuration of the magnetic field. Electron emission fluxes of lower-energy electrons increase after the peak, which indicates magnetic field trapping and accumulation in ropes.

CONCLUSION

Observations in microwave emission have provided important insights into morphological properties of the March 25, 2024 circular flare. The flare's hard emission was demonstrated to be associated with the interaction between magnetic flux ropes. For the first time, a microwave spectrum of electron emission from a remote source has been obtained and a connection has been found between meter-wave emission and electron acceleration in the flare core. Thus, we have demonstrated the high diagnostic potential of SRH multiwave observations for studying events with relatively small temporal and spatial scales. In-depth study of the dynamics of microwave sources and their polarization and spectral properties in this flare will be the subject of our future work.

We thank A.A. Kuznetsov for useful discussions. Meshalkina N.S. and Chengming Tan are grateful to PIFI Group (Grant No. 2025PG0008). We also acknowledge the teams of SDO, GOES, the Nobeyama Observatory, RHESSI, Fermi, RSTN, CBS, MUSER, and the ISTP SB RAS Radio Astrophysical Observatory for providing data. The results were obtained using the Unique Research Facility "Radioheliograph" [https://ckp-rf.ru/catalog/usu/4138190/] and the equipment of Shared Equipment Center "Angara" [http://ckp-angara.iszf.irk.ru/].

The work was financially supported by the Ministry of Science and Higher Education of the Russian Federation.

REFERENCES

Altyntsev A., Lesovoi S., Globa M., Gubin A., Kochanov A., Grechnev V., Ivanov E., Kobets V., Meshalkina N., et al. Multiwave Siberian Radioheliograph. *Sol.-Terr. Phys.* 2020, vol. 6, iss. 2, p. 30. DOI: 10.12737/stp-62202003.

Altyntsev A.T., Meshalkina N.S., Sych R.A., Kolotkov D.Y. Double peak quasi-periodic pulsations in a circular-ribbon flare. *Astron. Astrophys.* 2022, vol. 663, id. A149, 8 p. DOI: 10.1051/0004-6361/202243144.

Aschwanden M.J. *Physics of the Solar Corona: An Introduction.* Springer-Verlag; Praxis, 2004, 842 p.

Brown J.C., Melrose D.B., Spicer, D.S. Production of a collisionless conduction front by rapid coronal heating and its role in solar hard X-ray bursts. *Astrophys. J.* 1979, part 1, vol. 228, pp. 592–597. DOI: 10.1086/156883.

Chen X., Yan Y., Tan B., Huang J., Wang W., Chen L., et al. Quasi-periodic pulsations before and during a solar flare in AR 12242. *Astrophys. J.* 2019, vol. 878, no. 2, p. 78. DOI: 10.3847/1538-4357/ab1d64.

Dulk G.A., Marsh K.A. Simplified expressions for the gyrosynchrotron radiation from mildly relativistic, nonthermal and thermal electrons. *Astrophys. J.* 1982, vol. 259, p. 350. DOI: 10.1086/160171.

Fleishman G.D., Melnikov V.F. Gyrosynchrotron emission from anisotropic electron distributions. *Astrophys. J.* 2003, vol. 587, iss. 2, pp. 823–835. DOI: 10.1086/368252.

Guidice D.A., Cliver E.W., Barron W.R., Kahler S. The Air Force RSTN System. *Bull. of the American Astronomical Society.* 1981, vol. 13, p. 553.

Kumar P., Nakariakov V.M., Cho K.S. Observation of a quasiperiodic pulsation in hard X-ray, radio, and extreme-ultraviolet wavelengths. *Astrophys. J.* 2016, vol. 822, no. 1, p. 7. DOI: 10.3847/0004-637X/822/1/7.

Ledenev V.G. Generation of electromagnetic radiation by an electron beam with a bump on the tail distribution function. *Solar Phys.* 1998, vol. 179, iss. 2, pp. 405–420. DOI: 10.1023/A:1005007026541.

Lee J., White S.M., Chen X., Chen Y., Ning H., Li Bo, Masuda S. Microwave study of a solar circular ribbon flare. *Astrophys. J. Lett.* 2020, vol. 901, p. L10. DOI: 10.3847/2041-8213/abb4dd.

Lemen J.R., Title A.M., Akin D.J., Boerner P.F, Chou C., Drake J.F., Duncan D.W., Edwards Ch.G., et al. The Atmospheric Imaging Assembly (AIA) on the Solar Dynamics Observatory (SDO). *Solar Phys*. 2012, vol. 275, no. 1-2, pp. 17–40. DOI: 10.1007/s11207-011-9776-8.

Lesovoi S.V., Altyntsev A.T., Ivanov E.F., Gubin A.V. A 96-antenna radioheliograph. *Res. Astron. Astrophys.* 2014, vol. 14, iss. 7, article id. 864–868. DOI: 10.48550/arXiv.1403.4748.

Lesovoi S.V., Kobets V. Correlation plots of the Siberian Radioheliograph. *Sol.-Terr. Phys*. 2017, vol. 3, iss. 1. pp. 19–25. DOI: arXiv:1705.10043.

Levin B.N., Melnikov V.F. Quasi-linear model for the plasma mechanism of narrow-band microwave burst generation. *Solar Phys*. 1993, vol. 148, iss. 2, pp. 325–340. DOI: 10.1007/ BF00645093.

Masson S., Pariat E., Aulanier G., Schrijver C.J. The nature of flare ribbons in coronal null-point topology. *Astrophys. J.* 2009, vol. 700, iss.1, pp. 559–578. DOI: 10.1088/0004-637X/700/1/559.

Meegan C., Lichti G., Bhat P.N., et al. The Fermi gamma-ray burst monitor. *Astrophys. J.* 2009, vol. 702. p. 791. DOI: 10.1088/0004-637X/702/1/791.

Meshalkina N.S., Uralov A.M., Grechnev V.V., Altyntsev A.T., Kashapova L.K. Eruptions of magnetic ropes in two homologous solar events of 2002 June 1 and 2: a key to understanding an enigmatic flare. *PASJ*. 2009, vol. 61, p. 791. DOI: 10.1093/pasj/61.4.791.

Meshalkina N.S., Altyntsev A.T. Heating manifestations at the onset of the 29 June 2012 flare. *Sol.-Terr. Phys*. 2024, vol. 10, iss. 3, pp. 11–17. DOI: 10.12737/stp-103202402.

Nakajima H., Nishio M., Enome S., Shibasaki K., Takano T., Hanaoka Y., Torii C., et al. The Nobeyama Radioheliograph. *Proc. IEEE.* 1994, vol. 82, p. 705.

Pontin D.I., Priest E.R., Galsgaard K. On the nature of reconnection at a solar coronal null point above a separatrix dome. *Astrophys. J.* 2013, vol. 774, iss. 2, article id. 154, 10 p. DOI: 10.1088/0004-637X/774/2/154.

Priest E.R., Titov V.S. Magnetic reconnection at three-dimensional null points. *Philosophical Transactions of the Royal Society of London Series.* 1996, vol. A354(1721), pp. 2951–2992. DOI: 10.1098/rsta.1996.0136.

Shang Z., Xu K., Liu Y., Wu Z., Lu G., Zhang Y. Y., et al. A broadband solar radio dynamic spectrometer working in the millimeter-wave band. *Astrophys. J. Suppl. Ser.* 2022, vol. 258, p. 25. DOI: 10.3847/1538-4365/ac4257.

Shang Z., Wu Z., Liu Y., Bai Yu, Lu G., Zhang Y. Y., et al. The calibration of the 35–40 GHz solar radio spectrometer with the new moon and a noise source. *Astrophys. J. Suppl. Ser.* 2023, vol. 268, p. 45. DOI: 10.3847/1538-4365/acee00.

Sun X, Hoeksema J.T, Liu Y, Aulanier G., Su Y., Hannah I.G., Hock R.A. Hot spine loops and the nature of a late-phase solar flare. *Astrophys. J.* 2013, vol. 778, iss. 2, p. 139. DOI: 10.1088/0004-637X/778/2/139.

Tan C.M., Yan Y.H., Tan B.L., Yoshimi N., Tanaka H., Enome S. Study of calibration of solar radio spectrometers and the quiet-Sun radio emission. *Astrophys. J.* 2015, vol. 808, p. 61. DOI: 10.1088/0004-637X/808/1/61.

Torii C., Tsukiji Y., Kobayashi S., et al. Full-automatic radiopolarimeters for solar patrol at microwave frequencies. *Proc. of the Research Institute of Atmospherics*. Nagoya University, 1979, vol. 26, pp. 129–132.

Uralov A.M., Lesovoi S.V., Zandanov V.G., Grechnev V.V. Dual-filament initiation of a coronal mass ejection: observations and model. *Solar Phys* 2002, vol. 208, iss. 1, pp. 69–90. DOI: 10.1023/A:1019610614255.

Vlahos L., Papadopoulos K. On the upconversion of ion-sound to Langmuir turbulence. *Astrophys. J.* 1979, Part 2. Letters to the Editor, vol. 234, Dec. 15, 1979, pp. L217, L218. Navy-supported research. DOI: 10.1086/183143.

Yan Y., Zhang J.,Wang W., Liu F., Chen Z., Ji G. The Chinese Spectral Radioheliograph — CSRH. *Earth, Moon, and Planets*. 2009, vol. 104, iss. 1-4, pp. 97–100. DOI: 10.1007/ s11038-008-9254-y.

Yan Yihua, Chen Linjie, Yu Sijie. First radio burst imaging observation from Mingantu Ultrawide Spectral Radioheliograph. *IAUS.* 2016, vol. 320, pp. 427–435. DOI: 10.1017/S174392131600051X.

Wang Wei, Yan Yihua, Liu D., Chen Z., Su C., Liu F., et al. Calibration and data processing for a Chinese Spectral Radioheliograph in the decimeter wave range. *Publications Astronomical Society Japan*. 2013, vol. 65, iss. SP1, id. S18. DOI: 10.1093/pasj/65.sp1.S18.

Zhang Q. Circular-ribbon flares and the related activities. *Rev. Modern Plasma Physics*. 2024, vol. 8, iss. 1, article id. 7. DOI: 10.1007/s41614-024-00144-9.

Zhdanov D.A., Zandanov V.G. Broadband microwave spectropolarimeter. *Central European Astrophysical Bulletin.* 2011, vol. 35. p. 223.

Zheleznyakov V.V., Zlotnik E.Ya., Zaitsev V.V., Shaposhnikov V.E. Double plasma resonance and its manifestations in radio astronomy. *Physics-Uspekhi*. 2016, vol. 59, no. 10. DOI: 10.3367/UFNe.2016.05.037813.

URL: https://radiomag.iszf.irk.ru/books/sibirskii-radiogeliograf/page/sintez-radioizobrazenii-s-pomoshhiu-paketa-srh-synth (accessed June 25, 2025).

URL: https://badary.iszf.irk.ru/srhCorrPlot.php (accessed June 25, 2025).

URL: https://ckp-rf.ru/catalog/usu/4138190/ (accessed June 25, 2025).

URL: http://ckp-angara.iszf.irk.ru/ (accessed June 25, 2025).

The paper is based on material presented at the 20th Annual Conference on Plasma Physics in the Solar System, February 10–14, 2025, Space Research Institute of the Russian Academy of Sciences, Moscow, Russia.

Original Russian version: Altyntsev A.T., Meshalkina N.S., Anfinogentov S.A., Zhdanov D.A., Myshyakov I.I., Ivanov E.F., Chengming Tan, Zhao Wu., published in Solnechno-zemnaya fizika. 2025, vol. 11, no. 3, pp. 5–15. DOI: 10.12737/szf-113202501. © 2025 INFRA-M Academic Publishing House (Nauchno-Izdatelskii Tsentr INFRA-M).

How to cite this article

Altyntsev A.T., Meshalkina N.S., Anfinogentov S.A., Zhdanov D.A., Myshyakov I.I., Ivanov E.F., Chengming Tan, Zhao Wu. Processes of acceleration and transfer of electrons in a pulse circular ribbon flare. *Sol.-Terr. Phys*. 2025, vol. 11, iss. 3, pp. 3–12. DOI: 10.12737/stp-113202501.